PAPER

Check for updates

The effect of strong metal–support interaction (SMSI) on Pt–Ti/SiO$_2$ and Pt–Nb/SiO$_2$ catalysts for propane dehydrogenation†

Johnny Zhu Chen, [iD][a] Junxian Gao,[a] Paige R. Probus,[a] Wei Liu, [iD][b] Xianli Wu,[ac]
Evan C. Wegener,[d] A. Jeremy Kropf, [iD][d] Dmitry Zemlyanov, [iD][e]
Guanghui Zhang, [iD][f] Xin Yang*[ag] and Jeffrey T. Miller [iD]*[a]

In this study, we show how strong metal–support interaction (SMSI) oxides in Pt–Nb/SiO$_2$ and Pt–Ti/SiO$_2$ affect the electronic, geometric and catalytic properties for propane dehydrogenation. Transmission electron microscopy (TEM), CO chemisorption, and decrease in the catalytic rates per gram Pt confirm that the Pt nanoparticles were partially covered by the SMSI oxides. X-ray absorption near edge structure (XANES), *in situ* X-ray photoelectron spectroscopy (XPS), and resonant inelastic X-ray scattering (RIXS) showed little change in the energy of Pt valence orbitals upon interaction with SMSI oxides. The catalytic activity per mol of Pt for ethylene hydrogenation and propane dehydrogenation was lower due to fewer exposed Pt sites, while turnover rates were similar. The SMSI oxides, however, significantly increase the propylene selectivity for the latter reaction compared to Pt/SiO$_2$. In the SMSI catalysts, the higher olefin selectivity is suggested to be due to the smaller exposed Pt ensemble sites, which result in suppression of the alkane hydrogenolysis reaction; while the exposed atoms remain active for dehydrogenation.

1. Introduction

Supported metal nanoparticle catalysts are widely applied in petrochemical, refining and environmental technologies. Development of supported metal catalysts mainly focuses on optimizing the size, composition and geometry of the metal site to maximize the reaction rate, control selectivity and improve stability. Various porous materials with high surface areas are often used to support these metals in order to enhance the catalytic performance. Metal–support interaction is also important for tuning the catalytic properties.[1] Tauster,

et al. first reported significant interactions between group VIII metals and a TiO$_2$ support, where after high temperature reduction the adsorption of both H$_2$ and CO was suppressed. Other partially reducible oxides, such as Nb$_2$O$_5$,[2] CeO$_2$[3] and FeO$_x$,[4] also exhibit strong-metal support interactions (SMSI). It is generally recognized that the metal nanoparticles are encapsulated by oxide over layers blocking access to the nanoparticle surface. The SMSI encapsulation state is thought to occur by reduction of the oxide support to sub-stoichiometric oxides, which migrate on top of the metal nanoparticles.[5]

The SMSI state alters the catalytic properties for many reactions resulting from changes in geometric and electronic properties, although quantification of these effects has been difficult.[6,7] Kang *et al.*[8] studied selective hydrogenation of acetylene to ethylene on TiO$_2$ added Pd catalysts. After reduction at 500 °C, the catalyst showed suppression of CO chemisorption. Their XPS and TPD results showed that the Pd surface was electronically modified leading to weaker adsorption of acetylene. Goodman *et al.*[9–11] showed that the Au bilayer structure on TiO$_2$ (110) surface causes significant changes to electronic properties. The partially reduced TiO$_2$ promoted the electron donation from Ti$^{\delta+}$ to Au, resulting in weaker CO bonding. Komaya *et al.*[12] found that covering Ru with amorphous TiO$_x$ lead to lower Fischer–Tropsch (F–T) activity, but higher selectivity towards long-chain hydrocarbons. Lewandowski *et al.*[13] reported that Pt/Fe$_3$O$_4$

[a] *Davidson School of Chemical Engineering, Purdue University, 480 Stadium Mall Drive, IN 47906, USA. E-mail: mill1194@purdue.edu*
[b] *Dalian Institute of Chemical Physics, Chinese Academy of Sciences, Dalian, Liaoning 116023, China*
[c] *College of Chemistry, Zhengzhou University, No. 100 Kexue Avenue, Zhengzhou, Henan 450001, China*
[d] *Chemical Science and Engineering Division, Argonne National Laboratory, 9700 S. Cass Avenue, Lemont, Illinois 60439, USA*
[e] *Birck Nanotechnology Center, Purdue University, 1205 W State St., West Lafayette, IN, 47907, USA*
[f] *State Key Laboratory of Fine Chemicals, PSU-DUT Joint Center for Energy Research, School of Chemical Engineering, Dalian University of Technology, Dalian 116024, China*
[g] *School of Chemical Engineering, Huaqiao University, Xiamen, Fujian 361021, China. E-mail: yangxin@hqu.edu.cn*
† Electronic supplementary information (ESI) available. See DOI: 10.1039/d0cy00897d

This journal is © The Royal Society of Chemistry 2020

Catal. Sci. Technol., 2020, **10**, 5973–5982 | **5973**

catalyst was promoted due to the encapsulation of Pt nanoparticles by FeO (111) film. CO adsorption was suppressed; while, the CO_2 production rate increased for CO oxidation.

Due to the complexity of metal oxide supported catalysts it has been difficult to quantify the metal–oxide interaction at the atomic level.[14] In this study we prepared Pt nanoparticles partially covered with TiO_x (or NbO_x) supported on SiO_2, which display significantly higher propylene selectivity for propane dehydrogenation compared to SiO_2 supported Pt nanoparticles of similar size. Structural characterization by extended X-ray absorption fine structure (EXAFS) and *in situ* synchrotron X-ray diffraction (XRD) confirm that the nanoparticles in the SMSI catalysts are monometallic Pt. CO chemisorption confirms that *ca.* 80% of the nanoparticle surface was covered by the SMSI oxides. Electronic properties were measured by X-ray absorption near edge structure (XANES), *in situ* X-ray photoelectron spectroscopy (XPS), and resonant inelastic X-ray scattering (RIXS), confirming there are no significant changes in the energy of the Pt 5d valence orbitals. The SMSI oxides decrease the catalyst rate per gram for ethylene hydrogenation and propane dehydrogenation with little change in the turnover rate (TOR). For the latter reaction, however, the Pt-SMSI oxide catalysts displayed higher olefin selectivity, which is suggested to result from a decrease in the number of ensemble sites responsible for hydrogenolysis.

2. Materials and methods

2.1 Materials

Davisil 636 silica gel (99%), $Pt(NH_3)_4(NO_3)_2$ (99.995%), titanium(ιv) bis(ammonium lactato)dihydroxide (50% solution), niobium(v) ethoxide solution (99.95% trace metal basis), 200 proof ethyl alcohol were purchased from Sigma-Aldrich and used without further purification. The gases used for the catalytic testing were purchased from Indiana Oxygen Company, and the C_3H_8 is 5% balanced with N_2. The H_2 was also 5% balanced with N_2. Ultra-high purity gases were N_2 (99.999%) and He (99.98%). The gases used for XAS and XRD experiments were purchased from AirGas, Illinois, and all the gases were balanced with He.

2.2 Catalyst preparation

The monometallic Pt catalyst with 2 wt% Pt loading was prepared by a pH adjusted incipient wetness impregnation method (IWI) on SiO_2. $Pt(NH_3)_4(NO_3)_2$ was dissolved in 2 mL deionized water and ammonium hydroxide solution was added to adjust the pH to 11. The solution was added dropwise to Davisil Grade 636 silica (pore size = 60 Å, surface area = 480 m^2 g^{-1}). This catalyst was then dried overnight at 125 °C and calcined at 225 °C for 3 h. Finally, the catalyst was reduced in 5% H_2/N_2 (100 mL min^{-1}) at 200 °C for 30 min and 550 °C for 30 min.

A series of Pt–Ti bimetallic catalysts supported on SiO_2 with a target Pt loading of 2 wt% were synthesized by a sequential incipient wetness impregnation method (IWI). Various amounts of titanium(ιv) bis(ammonium lactato) dihydroxide solution (50% solution) (corresponding to 3, 6 and 8 wt% of Ti on SiO_2) were dissolved in deionized water and added dropwise to Davisil Grade 636 silica. The obtained Ti/SiO_2 was dried overnight at 125 °C and calcined at 300 °C for 3 h. A second solution was made using 0.2 g of $Pt(NH_3)_4(NO_3)_2$ dissolved in 2 mL deionized water and 1.0 mL of 30% ammonium hydroxide solution was added to adjust the pH to 11. The solution was added dropwise to the obtained Ti/SiO_2 precursor. This catalyst was then dried overnight at 125 °C and calcined at 225 °C for 3 h. Finally, the catalyst was reduced in 5% H_2/N_2 (100 mL min^{-1}) at 200 °C for 30 min and 550 °C for 30 min.

A similar method was followed to synthesize Pt–Nb bimetallic catalysts supported on SiO_2 with a target Pt loading of 2 wt%. Various amounts of niobium(v) ethoxide solution (99.95% trace metal basis) (corresponding to 2, 4 and 8 wt% of Nb on SiO_2) were dissolved in 200 proof ethyl alcohol and added dropwise to Davisil Grade 636 silica. The obtained Nb/SiO_2 was dried overnight at 125 °C and calcined at 550 °C for 3 h. A second solution was made using 0.2 g of $Pt(NH_3)_4(NO_3)_2$ dissolved in 2 mL deionized water and 1.0 mL of 30% ammonium hydroxide solution was added to adjust the pH to 11. The solution was added dropwise to the obtained Nb/SiO_2 precursor. This catalyst was then dried overnight at 125 °C and calcined at 225 °C for 3 h. Finally, the catalyst was reduced in 5% H_2/N_2 (100 mL min^{-1}) at 200 °C for 30 min and 550 °C for 30 min.

2.3 Scanning transmission electron microscopy (STEM)

The STEM images were taken at Dalian Institute of Chemical Physics using JEM-ARM200F equipped with EDS analyzer (200 kV, probe Cs-corrector, <1 Å spatial resolution). Samples were ground to fine powders and dispersed in isopropyl alcohol. One drop of the solution was added onto an ultrathin carbon film-Au TEM ready grid (TedPella) and dried on a hot plate at 70 °C. STEM images were taken using the high angle annular dark field (HAADF) detector at 200 kV with signal collection angle of 68–174 mrad. The particle size statistic was performed using the Image J program. A minimum of 200 particles were counted to obtain the size distribution for each catalyst. The electron energy loss spectroscopy (EELS) analysis was performed under 200 kV on the ARM200F in the spectrum imaging mode using a converged beam in semi-angle of 40 mrad and core loss electrons for Pt O edge, Ti L edge were collected from scattering angle up to 63 mrad over the energy range of 30–542 eV. Since there is risk that for ~2 nm particles the strong electron beam irradiation during EELS signal collection could result in particle reconstruction, particularly in the seriously

5974 | *Catal. Sci. Technol.*, 2020, **10**, 5973–5982

This journal is © The Royal Society of Chemistry 2020

charged environment of SiO_2-supported samples, we used single frame scanning to obtain EELS spectrum image to be able to capture the original structure before the samples reconstructed. The relatively weak counts of energy loss electrons were only utilized to extract structural information of the Pt–Ti sample, rather than its electronic state, which has been more precisely analyzed through multiple X-ray absorption techniques in this work.

2.4 *In situ* X-ray absorption spectroscopy (XAS)

In situ XAS experiments were performed at the 10-BM-B beamline at the Advanced Photon Source (APS), Argonne National Laboratory at the Pt L_3 (11.564 keV) edge in transmission mode, with energy step of 0.3 eV and energy precision better than 0.1 eV. Catalysts were ground into a powder, pressed into a sample holder, and sealed in a sample cell with leak-tight Kapton end caps. The sample cell was treated with 3.5% H_2/He for 30 minutes at 550 °C. The cell was cooled to room temperature in flowing He between each temperature exposure, sealed, and moved to the beamline to acquire data. The helium tank was connected to a gas purifier to reduce the possibility of O_2 exposure during cooling.

Each measurement was accompanied by simultaneous measurement of a Pt foil scan obtained through a third ion chamber for internal energy calibration. XAS data was fitted by using Demeter 0.9.25 software package. The edge energy was determined using the maximum of the first peak in the first derivative of the leading edge of the XANES spectrum. Least-squares fit in *R*-space of the k^2-weighted Fourier transform data from 2.7 to 12.0 Å^{-1} was used to obtain the EXAFS coordination parameters. The first shell was used to fit the EXAFS spectra. The amplitude reduction factor (S_0^2) was determined as 0.80 by fitting a reference spectrum of the Pt foil, and then it was used for fitting of all the other EXAFS spectra.

2.5 *In situ* X-ray diffraction (XRD)

In situ XRD measurements were performed at the 11-ID-C beamline at the APS, using X-rays of = 0.1173 Å (105.715 keV) and data was acquired using a Perkin-Elmer large area detector. Samples were pressed into a self-supported pellet (<2 mm thickness) and then loaded into a thermal stage. The cell was purged with He before a flow of 3.5% H_2/He at 100 ccm was introduced and the temperature was increased to 550 °C. After diffraction measurements were completed at the reduction temperature, the cell was cooled to 35 °C and a second diffraction measurement was obtained. The background scattering of the empty cell and the cell with silica were obtained under the same conditions and subtracted from the XRD pattern. The diffraction patterns were collected as 2-D Scherrer rings and were integrated using Fit2D software to obtain 1-D diffraction patterns as scattering intensity *vs.* 2θ plots.

2.6 X-ray photoelectron spectroscopy (XPS)

Kratos Axis Ultra DLD spectrometer was used to collect XPS data. Monochromic Al Kα radiation (1486.6 eV) at pass energy of 20 and 160 eV for high-resolution and survey spectra was used, respectively. To achieve better resolution and to avoid non-homogeneous electric charge of non-conducting powder, a commercial Kratos charge neutralizer was used. 2%Pt/SiO_2, 2%Pt–8%Nb/SiO_2 and 2%Pt–6%Ti/SiO_2 catalysts were directly loaded onto a sample holder. Reduction was performed in a reaction chamber attached to the spectrometer by heating the samples to 550 °C in 5% H_2/ Ar and holding for 30 minutes before cooling and evacuation. The XPS data were collected on reduced samples after they were transferred in vacuum (without exposure to air) to the spectrometer sample stage. XPS data were analyzed with CasaXPS software version 2313 Dev64 (www.casaxps.com). Curve-fitting was performed using Gaussian/Lorentzian peak shapes with a dampening parameter following a linear or Shirley background subtraction.

2.7 Resonant inelastic X-ray scattering (RIXS)

RIXS measurements were performed at the MR-CAT 10-ID beamline at the APS, Argonne National Lab. The catalyst was ground into a powder and pressed into a self-supported wafer in a stainless-steel sample holder at a 45° angle to the incident beam. The sample holder was placed in a resistively-heated reactor cell through which gases could be flowed.[15] Samples were reduced at 550 °C in 3% H_2/He at 50 cc min^{-1} for 20 min and then cooled to 200 °C in the same gas flow for measurement.

A spectrometer based on the Laue geometry was used for RIXS measurements and has been described previously.[16] Briefly, a cylindrically bent silicon crystal analyzer (ρ = 350 mm, Si thickness 55 μm, [100] wafer normal, <133> reflection) was used to select the Lβ_5 emission line of Pt. Fluorescence X-ray were detected using a Pilatus 100k pixel area detector. Soller slits between the analyzer and detector lowered the background signal by absorbing unreflected X-rays. The entire emission spectrum was collected at each incident energy; both the analyzer and detector positions were fixed during measurements.

2.8 CO chemisorption

CO chemisorption was performed on a Micromeritics ASAP 2020 chemisorption instrument. A U-shaped quartz reactor was used and approximately 0.1 g of catalysts was loaded in it. 5% H_2/He was introduced into the reactor at 50 ccm to reduce the catalysts at 550 °C or 225 °C and cooled to RT. He was flushed for 30 min before evacuation and measurements. The catalyst dispersion was obtained by difference analysis in the chemisorption curve. A stoichiometry of CO : Pt = 1 : 1 was assumed to calculate the dispersion for the catalysts.

This journal is © The Royal Society of Chemistry 2020

Catal. Sci. Technol., 2020, **10**, 5973–5982 | **5975**

Paper

Catalysis Science & Technology

2.9 Propane dehydrogenation and ethylene hydrogenation catalytic performance tests

Catalyst performance tests were performed in a fixed bed, quartz reactor with 3/8 inch OD. A K-type thermocouple (O.D. = 3.2 mm) was placed in the center of the catalyst bed to measure the temperature of the catalyst. A furnace connected to a controller was used to maintain the desired temperature. The weight of the catalyst (particle size 250–500 μm) loaded into the reactor ranged from 10 mg to 200 mg to vary the initial conversion and was diluted with silica to reach a total of 1 g. Prior to the reaction, the catalyst was reduced for 30 minutes at 550 °C under 100 ccm 5% H_2/N_2. For propane dehydrogenation, the reaction was performed in 2.5% C_3H_8, 2.5% H_2, balanced with N_2 at 550 °C. For ethylene dehydrogenation, the catalysts were pre-reduced at 550 °C and the reaction was performed in 2% C_2H_4, 2% H_2, balanced with N_2 at 30 °C. The products were analyzed with a Hewlett Packard 6890 series gas chromatograph using a flame ionization detector (FID) with a Restek Rt-Alumina Bond/Na_2SO_4 GC column (30 m in length, 0.32 mm ID, and 0.5 μm film thickness).

3. Results

3.1 Catalyst synthesis

Catalysts were prepared by addition of Ti and Nb oxides onto SiO_2 followed by addition and reduction of Pt to produce nanoparticles (NP) of approximately the same 2 nm size. The SMSI oxides were added by incipient wet impregnation of organometallic precursors (titanium(ıv) bis(ammonium lactato)dihydroxide in H_2O and niobium ethoxide in ethanol), followed by drying and calcination at 550 °C to remove the organic ligands. The titanium loading were 3, 6 and 8 wt%, and the niobium loadings were 4 and 8 wt%. To the SMSI-SiO_2 supports and unmodified SiO_2, $Pt(NH_3)_2(NO_3)_2$ dissolved in water with the pH adjusted to approximately 11 was impregnated, dried, calcined at 225 °C. The catalysts were reduced at 200 and 550 °C. The Pt loadings were 2 wt%.

3.2 CO chemisorption

The Pt dispersions of the catalysts were determined by CO chemisorption. Dispersions after reduction at 250 °C and 550 °C are shown in Table 1. After reduction at 250 °C, the Pt–Ti/SiO_2 (45–52%) and Pt–Nb/SiO_2 (53–57%) dispersions were similar to Pt/SiO_2 (55%) suggesting all catalysts have NPs of

Table 1 Summary of CO chemisorption results

Sample name	% dispersion 250 °C reduction	% dispersion 550 °C reduction
2Pt/SiO_2	55	45
2Pt–3Ti/SiO_2	52	12
2Pt–6Ti/SiO_2	50	10
2Pt–8Ti/SiO_2	45	8
2Pt–4Nb/SiO_2	57	9
2Pt–8Nb/SiO_2	53	7

approximately the same size. After reduction at 550 °C, however, Pt–Ti/SiO_2 and Pt–Nb/SiO_2 dispersions decreased significantly, *ca.* 7–12%, much smaller than that of 2Pt/SiO_2 (45%). The low chemisorption capacity after 550 °C reduction is characteristic of an SMSI effect of Pt NPs supported on TiO_2 and Nb_2O_5.[17]

3.3 TEM

The STEM average particle size distributions of Pt/SiO_2, Pt–6Ti/SiO_2 and Pt–8Nb/SiO_2 after reduction at 550 °C were 2.5, 1.7 and 1.5 nm, respectively (Table 2). The microstructure of 2Pt–6Ti/SiO_2 was studied *via* STEM and EELS methods as shown in Fig. 1. The nanoparticles having an average size of 1–2 nm were evenly dispersed on the SiO_2 support (Fig. 1A). These nanoparticles are single crystal in nature, without any shape anisotropy, as demonstrated in the magnified HAADF image (Fig. 1B). The primary structure matrix of the particles coincides quantitatively with the lattice pattern of metallic platinum (Fig. 1C) and slight compressive strain exists that is ascribed to the small size. Few Pt single atoms disperse near to the particle surface (orange circles in Fig. 1C and D). The EELS analysis on the elemental distribution further confirms the particle matrix is metallic Pt; while, Ti oxide species are widely dispersed over the whole particle, forming a TiO_x@Pt core–shell configuration.

3.4 *In situ* X-ray absorption spectroscopy (XAS)

The Pt L_3 edge X-ray absorption near edge structure (XANES) and extended X-ray absorption fine structure (EXAFS) spectra of 2Pt/SiO_2, 2Pt–6Ti/SiO_2 and 2Pt–8Nb/SiO_2 are shown in Fig. 2. After 550 °C reduction, 2Pt/SiO_2 had an edge energy of 11 564.0 eV, identical to Pt foil and consistent with monometallic Pt nanoparticles. For 2Pt–6Ti/SiO_2, the shape of the XANES spectra was similar to 2Pt/SiO_2; while, the XANES of 2Pt–8Nb/SiO_2 had a broader white line compared with 2Pt/SiO_2 due a slightly smaller particle size.[18] The edge energy, however, was identical to that of 2Pt/SiO_2 (Table 2).

The Pt L_3 EXAFS of 2Pt/SiO_2, shows three main peaks between 2–3 Å in the k^2-weighted magnitude of the Fourier transform, Fig. 2(B), which is typical for scattering in metallic Pt nanoparticles. 2Pt–6Ti/SiO_2 and 2Pt–8Nb/SiO_2 catalysts also showed similar peaks; while, the small size of the peaks suggests formation of slightly smaller nanoparticles. The k space and k^2-weighted Fourier transformation imaginary part spectra of the SMSI catalysts are also similar to Pt/SiO_2 (Fig. S1A†), and suggest that the SMSI catalysts are monometallic Pt nanoparticles. The EXAFS of the three catalysts were fit with a single Pt–Pt path and the results are shown in Table 1. The bond distance of the 2Pt/SiO_2 catalyst was 2.73 Å, and the coordination number was 8.9. The Pt nanoparticle size can be estimated from the coordination number, and is 2.5 nm for Pt/SiO_2, consistent with the STEM.[19] The bond distance of 2Pt–6Ti/SiO_2 and 2Pt–8Nb/SiO_2 was 2.71, slightly shorter than 2Pt/SiO_2. The coordination numbers of 2Pt–6Ti/SiO_2 and 2Pt–8Nb/SiO_2 are 7.8 and 6.6, respectively. The

Table 2 XANES edge energy and EXAFS fitting parameters for the catalysts

Sample name	XANES energy (eV)	$CN_{Pt–Pt}$	R, (Å)	σ^2 (Å^2)	Est. XAS size (nm)[19]	STEM size (nm)
2Pt/SiO$_2$	11 564.0	8.9 ± 0.5	2.74 ± 0.02	0.007	2.5	2.5
2Pt–6Ti/SiO$_2$	11 564.0	7.8 ± 0.3	2.71 ± 0.03	0.008	1.8	1.7
2Pt–8Nb/SiO$_2$	11 564.0	6.6 ± 0.2	2.71 ± 0.03	0.008	1.1	1.5

estimated particle sizes are given in Table 2 and are consistent with those determined by STEM.

3.5 *In situ* X-ray diffraction

In situ synchrotron X-ray diffraction (XRD) was used to confirm the crystalline phase of 2Pt–6Ti/SiO$_2$ and 2Pt–8Nb/SiO$_2$. Diffraction patterns were obtained at room temperature after *in situ* reduction at 550 °C. The patterns were obtained by subtracting the scattering of the empty cell, the silica support, and the gases in the X-ray path from the full diffraction patterns of the catalyst. The energy of the synchrotron X-ray beam is 105.715 keV, thus, the diffraction pattern occurs at smaller 2 theta angles compared to lab XRD
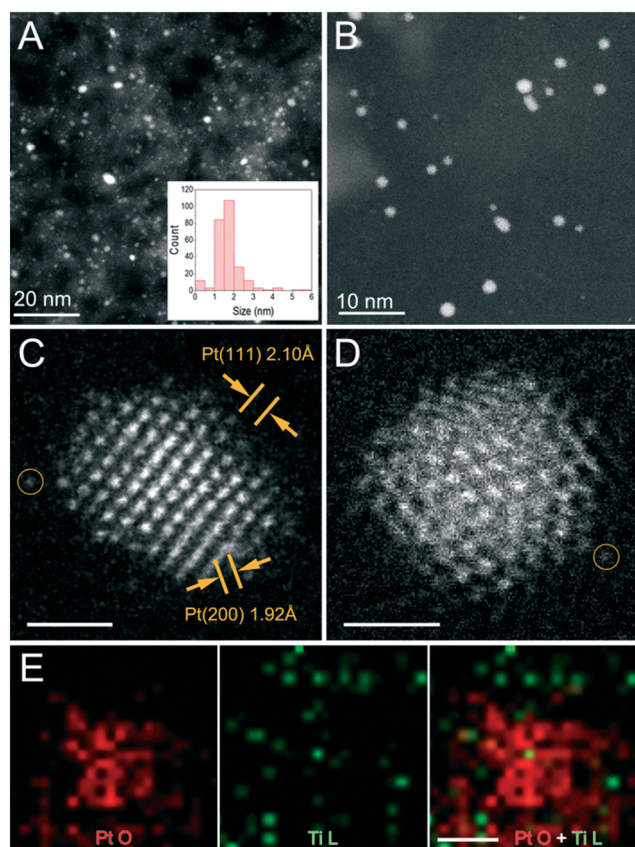

Fig. 1 (A) Representative low magnified dark-field STEM image of 2Pt–6Ti/SiO$_2$ in large field of view, inset the particle size statistic; (B) the magnified HAADF image disclosing the single-crystal nature of PtTi particles; (C) the high resolution HAADF image of one PtTi particle showing similar structure with platinum, suspended Pt single atom is marked with orange circle; (D) another PtTi nanoparticle and its corresponding elemental distribution (E) as revealed *via* EELS spectrum imaging. Scale bar in (C)–(E), 1 nm.
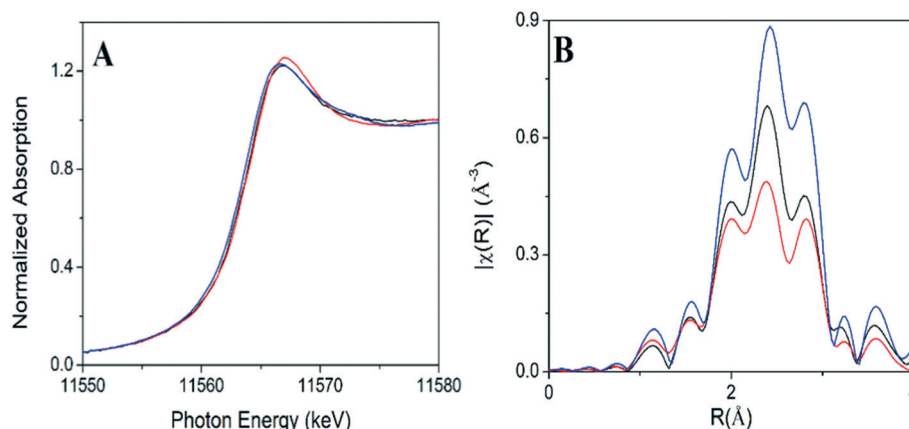
patterns. The 2θ peak of the (200) plane of FCC Pt, for example, is 3.43° rather than 46.0° in the standard lab XRD (Cu Kα = 8.04 keV). 2Pt/SiO$_2$ showed peaks at 2θ of 2.980°, 3.430°, 4.881°, and 5.712° corresponding to the (111), (200), (220) and (311) planes of the Pt FCC structure, respectively. For 2Pt–6Ti/SiO$_2$ and 2Pt–8Nb/SiO$_2$, there were similar cubic patterns at the same 2θ (Fig. 3). The patterns of the 2Pt–6Ti/SiO$_2$ and 2Pt–8Nb/SiO$_2$ catalysts, however, were broader than 2Pt/SiO$_2$. This is due to the slightly smaller particle size of the nanoparticles, which is consistent with the EXAFS and STEM results, and suggests that 2Pt–6Ti/SiO$_2$ and 2Pt–8Nb/SiO$_2$ formed monometallic Pt FCC structures with small particle sizes.

3.6 *In situ* XPS

In situ XPS measurement was performed on 2Pt/SiO$_2$, 2Pt–6Ti/SiO$_2$ and 2Pt–8Nb/SiO$_2$ reduced at 550 °C and measured without exposure to air. The Pt 4f region consists of two components corresponding to Pt 4f$_{7/2}$ and Pt 4f$_{5/2}$, respectively. The Pt NP's on 2Pt/SiO$_2$ showed Pt 4f$_{7/2}$ and 4f$_{5/2}$ binding energies of 71.7 eV and 75.0 eV respectively, which are assigned to metallic Pt. The Pt 4f$_{7/2}$ peak of 2Pt–6Ti/SiO$_2$ and 2Pt–8Nb/SiO$_2$ were at the same energy as 2Pt/SiO$_2$, (Fig. 4) indicating that Pt in 2Pt–6Ti/SiO$_2$ and 2Pt–8Nb/SiO$_2$ were in metallic state, and there was no significant electronic interaction between Pt and SMSI oxides.

Ti 2p XPS spectra of 2Pt–3Ti/SiO$_2$ and 2Pt–6Ti/SiO$_2$ catalyst were collected to analyze the chemical states of titanium (Fig. S2†). Curve fitting gives two species in both catalysts with different ratios. In 2Pt–6Ti/SiO$_2$, the major Ti 2p$_{3/2}$ peak at 459.5 eV is Ti^{4+} (red solid line), which is assigned to the excess TiO$_2$. The smaller peak at 458.8 eV (blue line) indicates a lower oxidation state, which might be associated with the TiO$_x$ overlayer on Pt surface. The percentages of Ti^{4+} and Ti^{x+} ($x < 4$) are 83.2% and 16.8%, respectively. In 2Pt–3Ti/SiO$_2$, the percentages of these two species are 43.8% and 56.2%.

Nb 3d XPS spectrum of 2Pt–8Nb/SiO$_2$ (Fig. S3†) catalyst shows the presence of Nb^{5+} with the 3d$_{5/2}$ peak at 208.0 eV and the 3d$_{3/2}$ peak at 210.8 eV. Since the loading of Nb is 8%, which is much higher than the Pt loading, excess Nb$_2$O$_5$ contributes mostly to Nb spectrum, and no other Nb peaks were observed.

3.7 Resonant inelastic X-ray scattering (RIXS)

In situ RIXS spectra for 2Pt/SiO$_2$ and 2Pt–8Nb/SiO$_2$ were collected in order to measure the energy difference, or energy transfer (ΔE), between the filled and unfilled Pt 5d states. The energy transfer is the difference in energy of the Pt L$_3$

This journal is © The Royal Society of Chemistry 2020

Catal. Sci. Technol., 2020, **10**, 5973–5982 | **5977**

Fig. 2 (A) Pt L_{III} edge XANES spectra of 2Pt/SiO$_2$ (blue), 2Pt–6Ti/SiO$_2$ (black) and 2Pt–8Nb/SiO$_2$ (red). (B) k^2-Weighted Fourier transformation magnitude of the Pt L_{III} edge EXAFS spectra of 2Pt/SiO$_2$ (blue), 2Pt–6Ti/SiO$_2$ (black) and 2Pt–8Nb/SiO$_2$ (red), Fourier transformation k range 2.7–12 Å^{-1}.

XANES absorption and Lβ_5 emission energies, which were obtained as a function of incident photon energy.[20] The RIXS spectra for 2Pt/SiO$_2$ and 2Pt–8Nb/SiO$_2$ are presented in Fig. 5 as two-dimensional contour plots that show the energy transfer as a function of incident photon energy. For 2Pt/SiO$_2$, the red region represents the maximum RIXS intensity, which occurs at incident energy at 11 564.5 eV with ΔE = 3.0 eV. Thus, the energy of the filled 5d orbitals, which are responsible for catalysis is 11 561.5 eV. The position of maximum intensity and energy transfer of 2Pt–8Nb/SiO$_2$ are similar to Pt/SiO$_2$. Since the energy of the XANES of both catalysts are also identical, the RIXS indicates there is no change in the energy of the filled Pt 5d states, which are responsible for catalysis, due to interaction with the SMSI oxide.

3.8 Ethylene hydrogenation

The effect of SMSI on catalytic performance was determined for ethylene hydrogenation. The catalysts were reduced at 550 °C and the hydrogenation reactions were performed at 30 °C.

The relation between the reciprocal space velocity and conversion for 2Pt/SiO$_2$, 2Pt–6Ti/SiO$_2$ and 2Pt–8Nb/SiO$_2$ catalysts are shown in Fig. 6.

The rates per mol of catalyst for 2Pt/SiO$_2$, 2Pt–6Ti/SiO$_2$ and 2Pt–8Nb/SiO$_2$ are 1.26 mol s^{-1} mol^{-1} Pt, 0.26 mol s^{-1} mol^{-1} Pt and 0.36 mol s^{-1} mol^{-1} Pt, respectively. The lower rates per g Pt after high temperature reduction is consistent with SMSI of Pt/TiO$_2$. The turnover rates (TOR), based on CO chemisorption capacity (Table 1), were similar, 2.8, 2.6 and 2.1 s^{-1}, respectively, and are also consistent with the previous literature.[21–23]

3.9 Propane dehydrogenation

The catalytic performance was also determined for propane dehydrogenation at 550 °C. Propane was co-fed with hydrogen to increase the hydrogenolysis selectivity to light alkanes, *e.g.*, ethylene, ethane and methane, and provides a more severe test of the catalysts' olefin selectivity. Initial selectivity was determined by extrapolation to zero time on stream, *i.e.*, selectivity free of coke, and conversion are shown in Fig. 7 and Table 3.
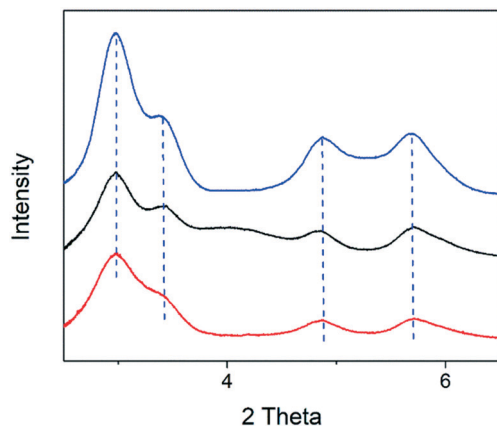

Fig. 3 *In situ* XRD patterns taken at 35 °C after reduction at 550 °C. 2Pt/SiO$_2$ (blue), 2Pt–6Ti/SiO$_2$ (black) and 2Pt–8Nb/SiO$_2$ (red).
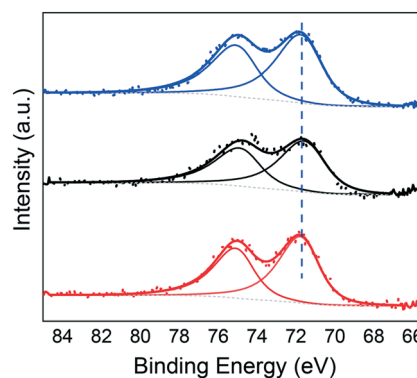

Fig. 4 Pt 4f XPS spectra of 2Pt/SiO$_2$ (blue), 2Pt–6Ti/SiO$_2$ (black) and 2Pt–8Nb/SiO$_2$ (red). Dots: experimental data; grey dashed line: background; solid line: fitted data.
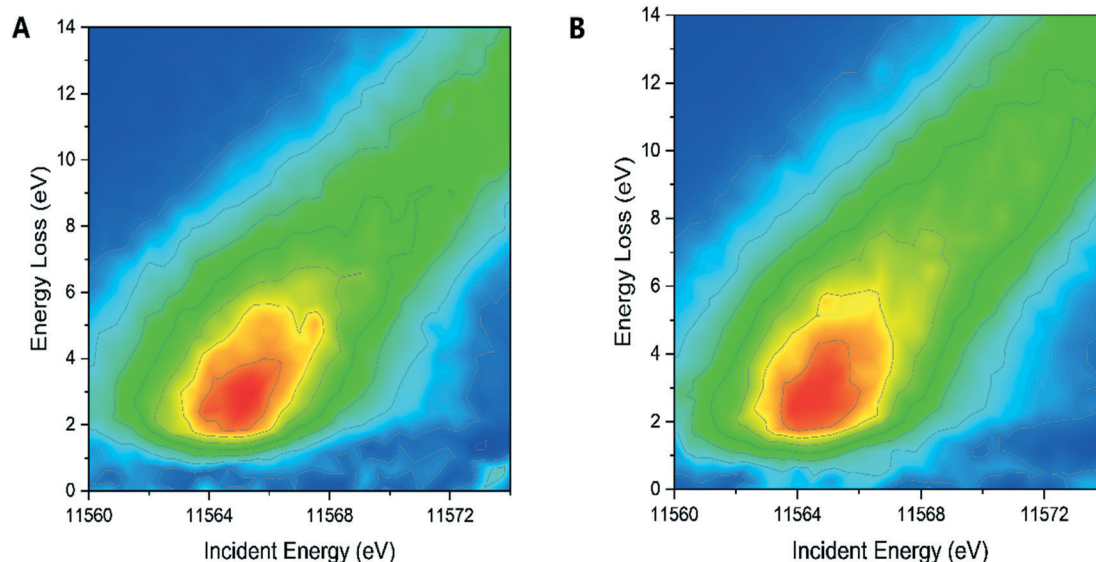
Fig. 5 RIXS planes for A) 2Pt/SiO$_2$ and B) 2Pt–8Nb/SiO$_2$.

Initial rates of the catalysts per mole Pt are shown in Table 3. Initial rates of Pt–Ti/SiO$_2$ and Pt–Nb/SiO$_2$ catalysts were 3–4 times lower than 2Pt/SiO$_2$. The TORs based on CO chemisorption were determined under differential conditions are also given in Table 3. The initial TORs for 2Pt/SiO$_2$, 2Pt–6Ti/SiO$_2$ and 2Pt–8Nb/SiO$_2$ catalysts, for example, were 0.17 s^{-1}, 0.22 s^{-1} and 0.19 s^{-1}, respectively. The initial TORs of Pt–Ti/SiO$_2$ and Pt–Nb/SiO$_2$ catalysts with higher SMSI loading were also similar to those of 2Pt/SiO$_2$, Table 3.

The propylene selectivity for 2Pt/SiO$_2$ at 10% conversion was *ca.* 70%. The selectivity decreased with increasing conversion. The propylene selectivity for 2Pt–6Ti/SiO$_2$, however, was near 95% at 10% conversion and only decreased slightly with increasing conversion (90% selectivity at 25% conversion). For 2Pt–8Nb/SiO$_2$, the selectivity at 10%

conversion was about 90% conversion and decreased slightly with increasing conversion (87% selectivity at 30% conversion). For different Ti and Nb loadings, shown in Table 3 and Fig. S4,† the propylene selectivities and product distributions were very similar to those in Fig. 7, suggesting the catalytic performance was not sensitive to the SMSI oxide loading. Thus, while the TOR of the SMSI catalysts were similar to those of Pt/SiO$_2$, the propane dehydrogenation selectivity was not typical of Pt NP's, *i.e.*, has a much higher olefin selectivity.

4. Discussion

4.1 Electronic and geometric effects of Pt–Nb/SiO$_2$ and Pt–Ti/SiO$_2$

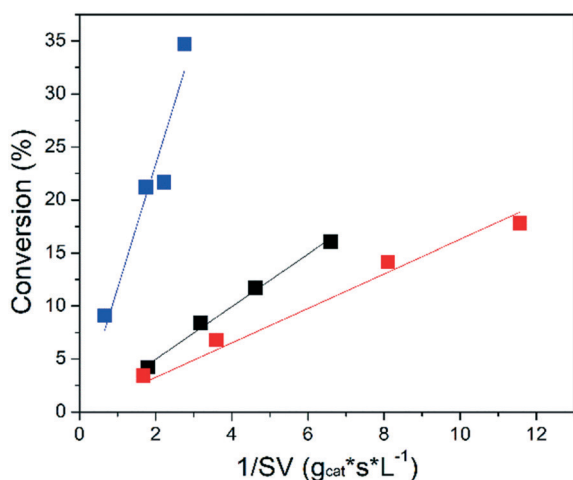The structure and catalytic properties of noble metals on SMSI oxides have been extensively studied. The strong metal–

Fig. 6 Ethylene conversion at different space velocities of 2Pt/SiO$_2$ (blue), 2Pt–3Ti/SiO$_2$ (black) and 2Pt–8Nb/SiO$_2$ (red) reduced at 550 °C. Reaction conditions: 30 °C, 2% C$_2$H$_6$ + 2% H$_2$ balanced with N$_2$.
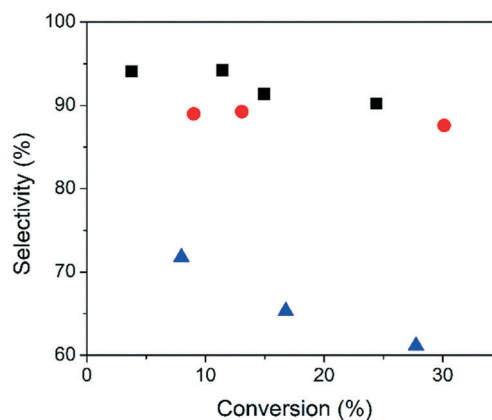

Fig. 7 Propylene selectivity at different conversions of 2Pt/SiO$_2$ (blue triangle), 2Pt–6Ti/SiO$_2$ (black square) and 2Pt–8Nb/SiO$_2$ (red circle). Reaction conditions: 550 °C, 2.5% C$_3$H$_8$ + 2.5% H$_2$ balanced with N$_2$.

This journal is © The Royal Society of Chemistry 2020

Catal. Sci. Technol., 2020, **10**, 5973–5982 | 5979

Table 3 Summary of catalytic results for propane dehydrogenation

Sample name	% selectivity				Rate (mol s^{-1} mol^{-1} catalyst)	Initial turnover rate (s^{-1})
	C_3H_6	CH_4	C_2H_4	C_2H_6		
2Pt/SiO$_2$	70	22	3	1	0.077	0.17
2Pt–3Ti/SiO$_2$	93	5	1	Trace	0.019	0.16
2Pt–6Ti/SiO$_2$	93	5	1	Trace	0.022	0.22
2Pt–8Ti/SiO$_2$	94	4	1	Trace	0.017	0.22
2Pt–4Nb/SiO$_2$	88	9	2	Trace	0.025	0.28
2Pt–8Nb/SiO$_2$	91	6	2	Trace	0.013	0.19

Reaction conditions: 550 °C, 2.5% C_3H_8 + 2.5% H_2 balanced with N_2; selectivity and TOR calculated at 10% C_3H_8 conversion; TOR calculated based on C_3H_8 conversion rate.

support interaction often leads to stabilization of small particle size, reduction of H_2 and CO chemisorption capacity and altered catalytic properties.[5] Coverage of the NP by the support can lead to higher or lower rate and altered selectivity. The latter are often suggested to be due to changes in the electronic properties of the metal NPs, often described as electron transfer to metal from a partially reduced support oxide.[24,25] For example, the XPS Pt $4f_{7/2}$ peak is shifted from 71.0 eV (Pt) to 70.2 eV (Pt/TiO$_2$) suggesting that Pt interacts with the TiO$_2$ support, which provided electrons to the surface of the nanoparticles; i.e., Pt gains electrons from the partially reduced support. Ruppert et al., demonstrated that addition of ZrO$_2$ to Pt/TiO$_2$ improved the selective hydrogenation of crotonaldehyde by controlling the extent of SMSI coverage after reduction at 500 °C. Addition of ZrO$_2$ appears to inhibit full coverage by TiO$_x$ leading to higher rates. For these catalysts, the Pt $4f_{7/2}$ binding energy was very similar to Pt, e.g., ~71.0 eV.[26] The improved catalyst selectivity was ascribed to the formation of interfacial active sites of Pt NPs with TiO$_x$ SMSI overlayers without full coverage and complete loss of activity.

Several studies of SMSI have shown evidence for electronic modification of the group VIII metal due to alloying. Haller et al. observed that for Rh/TiO$_2$ there is a shift in the Rh K-edge XANES thought to be due to formation of intermetallic Rh$_3$Ti alloy. EXAFS also showed that there was Rh–Ti scattering with the bond distance at 2.56 Å.[27,28] Liu et al. showed for Pt/FeO$_x$ that although the Pt nanoparticles were partially encapsulated, the catalytic activity was high for CO oxidation at 27 °C with TOR of 0.15 s^{-1} due to dual reaction sites (Pt for CO adsorption and reaction and FeO$_x$ for O$_2$ adsorption and activation).[4] For Pt/FeO$_x$ and Pd/FeO$_x$ shifts to lower energy in the 4f and 3d XPS, respectively, suggested that there was electron transfer from the FeO$_x$ to the noble metals increasing the electron density of the NPs.[4] In other studies, Fe has been shown to form alloys with Pt and Pd after reduction at 550 °C.[29,30] Thus, the electronic effect attributed to SMSI by FeO$_x$ may be due to alloy formation, rather than by the interaction with the Fe oxide over layers.

In this study, TEM, XAS and XRD show that these catalysts are monometallic Pt NPs, of approximately the same size, ca. 2 nm ± 0.5 nm. In addition, after reduction at 550 °C, TEM,

EELS, CO chemisorption and catalytic rates showed that the Pt nanoparticles were partially covered by the metal oxides similar to previous SMSI studies. CO chemisorption showed that 80% of the Pt nanoparticles' surface was covered by the SMSI oxides. For example, for 2Pt–6Ti/SiO$_2$ the dispersion after reducing at 250 °C (without SMSI) was 50% while after 550 °C the dispersion was 10%. This reduced the fraction of exposed, surface Pt atoms and led to lower activity per gram of catalyst for ethylene hydrogenation and propane dehydrogenation. The TORs of the Pt/SiO$_2$ and Pt–Ti/SiO$_2$ and Pt–Nb/SiO$_2$ catalysts, however, were very similar suggesting that there was no intrinsic change in the catalytic properties of Pt. While the TORs for propane dehydrogenation for Pt–Ti/SiO$_2$ and Pt–Nb/SiO$_2$ were similar to Pt/SiO$_2$, the olefin selectivity is significantly improved for SMSI modified Pt NPs.

SMSI oxides are often thought to transfer electron density from the partially reduced support to the metal NPs altering their catalytic performance. The electronic properties of Pt in the Pt–Ti/SiO$_2$, Pt–Nb/SiO$_2$ and Pt/SiO$_2$ were investigated by in situ XANES, XPS and RIXS. All catalysts had the same in situ XPS binding energies, for example, the Pt $4f_{7/2}$ was 71.7 eV. Similarly, the in situ XANES edge energy of all catalysts were identical (11 564.0 eV) and the same as Pt foil. While XPS and XANES spectra indicate no significant electronic changes, these are indirect measurements of the Pt filled 5d orbital energies, which are responsible for catalysis. The energy transfer determined by RIXS when combined with the XANES energies gives the energy of the Pt 5d filled states. Consistent with the XANES and XPS spectra, the energies of the Pt 5d filled orbitals are the same for 2Pt/SiO$_2$ and 2Pt–8Nb/SiO$_2$. Thus, there is no spectroscopic evidence that partial coverage of Pt NPs by TiO$_x$ and NbO$_x$ SMSI over layers leads to a change in the energy of the Pt 5d filled orbitals, and also suggests that the changes in propylene selectivity are not due to change in the chemical nature of the Pt NPs.

4.2 Structure–function relationship of Pt–Nb/SiO$_2$ and Pt–Ti/SiO$_2$ catalysts: the promotion effect of Nb and Ti

Dehydrogenation is a structure insensitive reaction, requiring individual atoms for catalytic activity. However, hydrogenolysis is a structure sensitive reaction, which

5980 | Catal. Sci. Technol., 2020, **10**, 5973–5982

This journal is © The Royal Society of Chemistry 2020

requires Pt ensembles as active sites.[31] High propylene selectivity in Pt₃Mn,[32] Pt₃Co,[33] Pt₃Cr,[34] Pt₃V[20] and Pt₁Zn₁[16] intermetallic alloys has been proposed to be due to isolated Pt and Pd or small ensemble sites. For example, in Pt₃M alloys there are 3-fold Pt ensembles, which have high olefin selectivity for alkane dehydrogenation. In alloy catalysts, in addition to changes in the ensemble size, there are also always electronic changes in the energy of the active metal valence orbitals. These electronic changes are also thought to be essential for high olefin selectivity.[35]

Pt–Ti/SiO₂ and Pt–Nb/SiO₂ had propylene selectivity ~90%, similar to alloy catalysts,[29,36–39] however, *in situ* EXAFS and XRD showed that these Pt NPs did not form alloys. In addition *in situ* XPS, XANES and RIXS show that there are no changes in the energy of the Pt valence orbitals, and is also consistent with monometallic Pt NPs. Thus, the high olefin selectivity likely results from a change in the average surface ensemble size. SMSI of supported noble metal catalysts are known to lower the rates of alkane hydrogenolysis. For example, Bracey *et al.* have shown that SMSI leads to lower ethane hydrogenolysis rates on Pd/TiO₂.[40] Similar suppression of hydrogenolysis selectivity was observed for NiMo/SiO₂ catalyst for HDO of *m*-cresol.[41] For the latter, Ni was also shown not to alloy with Mo. It seems likely, therefore, that the improved olefin selectivity of Pt–Ti/SiO₂ and Pt–Nb/SiO₂ results from partial coverage of 1–2 nm nanoparticles leaving a few and smaller surface ensembles and lower hydrogenolysis rates. In a recent study of PdZn, PdIn, Pd₂Ga, Pd₃Mn and Pd₃Fe intermetallic alloys with isolated Pd atoms (PdZn, PdIn) were more selective than structures with 3-fold ensemble sites (Pd₂Ga, Pd₃Mn and Pd₃Fe); however, the olefins selectivity of the latter was above 90% and much higher than monometallic Pd NPs. In addition, DFT modeling suggested that the hydrogenolysis ensemble consists of 4 Pd atoms in two adjacent 3-fold sites.[42] If a hydrogenolysis site contains 4 atoms, or more, then the approximate 80% surface coverage of the 1–2 nm Pt NPs catalysts by the SMSI oxide would be expected leave few ensemble sites. The remaining 20% of exposed Pt atoms, however, would remain active for dehydrogenation. Thus, the higher dehydrogenation selectivity appears to result from selective suppression of structure sensitive, hydrogenolysis reactions. The loss of surface sites does lead to lower rates per total mole of Pt, but the intrinsic catalytic properties of Pt NPs are unchanged. A similar interpretation to explain the selectivity due to partial surface adsorbate coverage on NP surfaces has recently been proposed.[43]

5. Conclusions

Pt–Ti/SiO₂ and Pt–Nb/SiO₂ catalysts showed SMSI behaviors consistent with previous studies of metal NPs on TiO₂ and Nb₂O₅. Several *in situ* characterizations showed no change in energy of the Pt 5d valance orbitals responsible for catalysis. Partial covering of the catalytic surface by the SMSI oxides resulted in lower activity per gram of Pt, but similar TORs,

for ethylene hydrogenation and propane dehydrogenation. The olefin selectivity for propane dehydrogenation, however, was significantly higher on the SMSI catalysts and is thought to be due to few hydrogenolysis ensembles on the SMSI oxide covered Pt nanoparticles; while the exposed Pt sites remain active for dehydrogenation.

Conflicts of interest

There are no conflicts to declare.

Acknowledgements

References

1 G. L. Haller and D. E. Resasco, *Adv. Catal.*, 1989, **36**, 173–235.

2 K. Tanabe, *Catal. Today*, 1990, **8**, 1–11.

3 A. Caballero, J. P. Holgado, V. M. Gonzalez-delaCruz, S. E. Habas, T. Herranz and M. Salmeron, *Chem. Commun.*, 2010, **46**, 1097–1099.

4 L. Q. Liu, F. Zhou, L. G. Wang, X. J. Qi, F. Shi and Y. Q. Deng, *J. Catal.*, 2010, **274**, 1–10.

5 S. J. Tauster, S. C. Fung, R. T. K. Baker and J. A. Horsley, *Science*, 1981, **211**, 1121–1125.

6 T. Ekou, L. Ekou, A. Vicente, G. Lafaye, S. Pronier, C. Especel and P. Marecot, *J. Mol. Catal. A: Chem.*, 2011, **337**, 82–88.

7 I. McManus, H. Daly, J. M. Thompson, E. Connor, C. Hardacre, S. K. Wilkinson, N. S. Bonab, J. ten Dam, M. J. H. Simmons, E. H. Stitt, C. D'Agostino, J. McGregor, L. F. Gladden and J. J. Delgado, *J. Catal.*, 2015, **330**, 344–353.

8 J. H. Kang, E. W. Shin, W. J. Kim, J. D. Park and S. H. Moon, *J. Catal.*, 2002, **208**, 310–320.

9 D. W. Goodman, *Catal. Lett.*, 2005, **99**, 1–4.

This journal is © The Royal Society of Chemistry 2020

Catal. Sci. Technol., 2020, **10**, 5973–5982 | **5981**

10 M. S. Chen and D. W. Goodman, *Top. Catal.*, 2007, **44**, 41–47.

11 M. Chen, Y. Cai, Z. Yan and D. W. Goodman, *J. Am. Chem. Soc.*, 2006, **128**, 6341–6346.

12 T. Komaya, A. T. Bell, Z. Wengsieh, R. Gronsky, F. Engelke, T. S. King and M. Pruski, *J. Catal.*, 1994, **149**, 142–148.

13 M. Lewandowski, Y. N. Sun, Z. H. Qin, S. Shaikhutdinov and H. J. Freund, *Appl. Catal., A*, 2011, **391**, 407–410.

14 D. R. Rainer, C. Xu and D. W. Goodman, *J. Mol. Catal. A: Chem.*, 1997, **119**, 307–325.

15 T. B. Bolin, T. P. Wu, N. Schweitzer, R. Lobo-Lapidus, A. J. Kropf, H. Wang, Y. F. Hu, J. T. Miller and S. M. Heald, *Catal. Today*, 2013, **205**, 141–147.

16 V. J. Cybulskis, B. C. Bukowski, H.-T. Tseng, J. R. Gallagher, Z. Wu, E. Wegener, A. J. Kropf, B. Ravel, F. H. Ribeiro, J. G. Greeley and J. T. Miller, *ACS Catal.*, 2017, **7**, 4173–4181.

17 P. Panagiotopoulou and D. I. Kondarides, *J. Catal.*, 2008, **260**, 141–149.

18 Y. Lei, J. Jelic, L. C. Nitsche, R. Meyer and J. T. Miller, *Top. Catal.*, 2011, **54**, 334–348.

19 J. T. Miller, A. J. Kropf, Y. Zha, J. R. Regalbuto, L. Delannoy, C. Louis, E. Bus and J. A. van Bokhoven, *J. Catal.*, 2006, **240**, 222–234.

20 S. Purdy, P. Ghanekar, G. M. Mitchell, A. J. Kropf, D. Y. Zemlyanov, Y. Ren, F. H. Ribeiro and W. N. Delgass, *ACS Appl. Energy Mater.*, 2020, **3**, 1410–1422.

21 R. D. Cortright, S. A. Goddard, J. E. Rekoske and J. A. Dumesic, *J. Catal.*, 1991, **127**, 342–353.

22 J. C. Schlatter and M. Boudart, *J. Catal.*, 1972, **24**, 482–492.

23 T. A. Dorling, M. J. Eastlake and R. L. Moss, *J. Catal.*, 1969, **14**, 23–33.

24 M. K. Bahl, S. C. Tsai and Y. W. Chung, *Phys. Rev. B: Condens. Matter Mater. Phys.*, 1980, **21**, 1344–1348.

25 J. Ohyama, A. Yamamoto, K. Teramura, T. Shishido and T. Tanaka, *ACS Catal.*, 2011, **1**, 187–192.

26 A. M. Ruppert and T. Paryjczak, *Appl. Catal., A*, 2007, **320**, 80–90.

27 D. E. Resasco, R. S. Weber, S. Sakellson, M. McMillan and G. L. Haller, *J. Phys. Chem.*, 1988, **92**, 189–193.

28 S. Sakellson, M. McMillan and G. L. Haller, *J. Phys. Chem.*, 1986, **90**, 1733–1736.

29 C. Yang, Z. Wu, G. Zhang, H. Sheng, J. Tian, Z. Duan, H. Sohn, A. J. Kropf, T. Wu, T. R. Krause and J. T. Miller, *Catal. Today*, 2018, **323**, 123–128.

30 E. C. Wegener, B. C. Bukowski, D. Yang, Z. Wu, A. J. Kropf, W. N. Delgass, J. Greeley, G. Zhang and J. T. Miller, *ChemCatChem*, 2020, **12**, 1–10.

31 M. Boudart, *J. Mol. Catal.*, 1985, **30**, 27–38.

32 Z. W. Wu, B. C. Bukowski, Z. Li, C. Milligan, L. Zhou, T. Ma, Y. Wu, Y. Ren, F. H. Ribeiro, W. N. Delgass, J. Greeley, G. H. Zhang and J. T. Miller, *J. Am. Chem. Soc.*, 2018, **140**, 14870–14877.

33 L. G. Cesar, C. Yang, Z. Lu, Y. Ren, G. H. Zhang and J. T. Miller, *ACS Catal.*, 2019, **9**, 5231–5244.

34 N. J. LiBretto, C. Yang, Y. Ren, G. H. Zhang and J. T. Miller, *Chem. Mater.*, 2019, **31**, 1597–1609.

35 J. J. Sattler, J. Ruiz-Martinez, E. Santillan-Jimenez and B. M. Weckhuysen, *Chem. Rev.*, 2014, **114**, 10613–10653.

36 C. Ye, Z. Wu, W. Liu, Y. Ren, G. Zhang and J. T. Miller, *Chem. Mater.*, 2018, **30**, 4503–4507.

37 Z. Wu, E. C. Wegener, H.-T. Tseng, J. R. Gallagher, J. W. Harris, R. E. Diaz, Y. Ren, F. H. Ribeiro and J. T. Miller, *Catal. Sci. Technol.*, 2016, **6**, 4503–4507.

38 E. C. Wegener, Z. Wu, H.-T. Tseng, J. R. Gallagher, Y. Ren, R. E. Diaz, F. H. Ribeiro and J. T. Miller, *Catal. Today*, 2018, **299**, 146–153.

39 J. Z. Chen, Z. W. Wu, X. B. Zhang, S. Choi, Y. Xiao, A. Varma, W. Liu, G. H. Zhang and J. T. Miller, *Catal. Sci. Technol.*, 2019, **9**, 1349–1356.

40 J. D. Bracey and R. Burch, *J. Catal.*, 1984, **86**, 384–391.

41 F. F. Yang, N. J. Libretto, M. R. Komarneni, W. Zhou, J. T. Miller, X. L. Zhu and D. E. Resasco, *ACS Catal.*, 2019, **9**, 7791–7800.

42 S. C. Purdy, R. R. Seemakurth, G. M. Mitchell, M. Davidson, B. Lauderback, S. Deshpande, Z. Wu, E. C. Wegener, J. P. Greeley and J. T. Miller, *Chem. Sci.*, 2020, 5066–5081.

43 J. C. Matsubu, S. Y. Zhang, L. DeRita, N. S. Marinkovic, J. G. G. Chen, G. W. Graham, X. Q. Pan and P. Christopher, *Nat. Chem.*, 2017, **9**, 120–127.

5982 | *Catal. Sci. Technol.*, 2020, **10**, 5973–5982

This journal is © The Royal Society of Chemistry 2020